Magnetism and crystalline electric field effect in $ThCr_2Si_2$-type $CeNi_2As_2$

Yongkang Luo,[1] Jinke Bao,[1] Chenyi Shen,[1] Jieke Han,[1] Xiaojun Yang,[1] Chen Lv,[1] Yuke Li,[2] Wenhe Jiao,[1] Bingqi Si,[1] Chunmu Feng,[1] Jianhui Dai,[2] Guanghan Cao,[1] and Zhu-an Xu[1,*]

[1]*Department of Physics and State Key Laboratory of Silicon Materials, Zhejiang University, Hangzhou 310027, China*

[2]*Department of Physics, Hangzhou Normal University, Hangzhou 310036, China*

(Received 19 August 2012; revised manuscript received 11 December 2012; published 26 December 2012)

A millimeter-sized $ThCr_2Si_2$-type $CeNi_2As_2$ single crystal was synthesized by the NaAs flux method and its physical properties were investigated by magnetization, transport, and specific-heat measurements. In contrast to the previously reported $CaBe_2Ge_2$-type $CeNi_2As_2$, the $ThCr_2Si_2$-type $CeNi_2As_2$ is a highly anisotropic uniaxial antiferromagnet with the transition temperature $T_N = 4.8$ K. A magnetic-field-induced spin-flop transition was seen below T_N when the applied **B** is parallel to the c axis, the magnetic easy axis, together with a huge frustration parameter $f = \theta_W/T_N$. A pronounced Schottky-type anomaly in specific heat was also found around 160 K, which could be attributed to the crystalline electric field effect with the excitation energies being fitted to $\Delta_1 = 325$ K and $\Delta_2 = 520$ K, respectively. Moreover, the in-plane resistivity anisotropy and low-temperature x-ray diffractions suggest that this compound is a rare example exhibiting a possible structure distortion induced by the $4f$-electron magnetic frustration.

DOI: 10.1103/PhysRevB.86.245130 PACS number(s): 74.70.Dd, 75.30.Gw, 75.30.Kz, 75.10.Dg

I. INTRODUCTION

The interest in the $ThCr_2Si_2$-type structure has been rekindled since the discovery of superconductivity (SC) in $(Ba_{1-x}K_x)Fe_2As_2$.[1] SC is also achieved when Ba is replaced by other alkaline-earth metals such as Ca and Sr or even the divalent rare-earth metal Eu, either by chemical doping or pressure effect.[2–8] On the other hand, the nickel-based pnictide, e.g., $BaNi_2As_2$, was reported to show SC too, although the nickels are nonmagnetic and the T_c is much lower.[9] In these 122-compounds formulated with ATm_2As_2 (A = Ca, Sr, Ba, or Eu, Tm = transition metals), two vertically reversed TmAs layers are sandwiched along the c axis, while the A atoms are embedded in-between, following a sequence of TmAs-A-TmAs. This crystalline structure constitutes a platform for understanding the interplay between Kondo interaction and Ruderman-Kittel-Kasuya-Yosida (RKKY) interaction if A is replaced by magnetic rare-earth metals. Indeed, the research for the $4f$-electron correlation in $ThCr_2Si_2$ structured compounds has been a long story, and a famous example is $CeCu_2Si_2$, the first heavy-fermion superconductor.[10] Therefore, it is very interesting to study the Ce-based 122-nickel pnictides such as $CeNi_2As_2$.

Remarkably, $CeNi_2As_2$ crystallizes in either $ThCr_2Si_2$ ($I4/mmm$, No.139) or $CaBe_2Ge_2$ ($P4/nmm$, No.129) structure [see Fig. 1(a)]. The main difference between them comes from the interchange of the Ni and As positions in one-half of the NiAs layers in the $CaBe_2Ge_2$-type $CeNi_2As_2$, which results in the loss of the inversion symmetry.[11] Previous studies on polycrystalline samples have revealed that the $ThCr_2Si_2$-type $CeNi_2As_2$ shows an antiferromagnetic (AFM) transition at around 5 K, while the $CaBe_2Ge_2$-type $CeNi_2As_2$ is a nonmagnetic Kondo lattice compound.[12] Single-crystalline samples are then highly desirable in order to further distinguish the properties of the two structures. However, since the occurrence of $ThCr_2Si_2$ type or $CaBe_2Ge_2$ type largely depends on the process of heat treatment,[13] and in many cases, a mixture of the two will be derived, the properties of $ThCr_2Si_2$-type $CeNi_2As_2$ are still not well understood.

In this article, we report the measurements on the magnetic, transport, and thermodynamic properties of the $ThCr_2Si_2$-type $CeNi_2As_2$ based on millimeter-sized single-crystalline samples. A single-crystalline sample of $CeNi_2As_2$ was successfully synthesized by the NaAs flux method. We find that $CeNi_2As_2$ is a highly anisotropic uniaxial antiferromagnet with the transition temperature $T_N = 4.8$ K. The Ce^{3+} moments are likely to align along the c axis. A magnetic-field-induced metamagnetic transition (MMT) was seen below T_N. A pronounced crystalline electric field (CEF) effect was observed. These magnetic and thermodynamic properties can be well understood by the CEF calculation, showing that the $j = \frac{5}{2}$ multiplet of Ce^{3+} splits into three Kramers doublets with the excitation energies $\Delta_1 = 325$ K and $\Delta_2 = 520$ K. In contrast to the $CaBe_2Ge_2$-type $CeNi_2As_2$, the Kondo effect in the $ThCr_2Si_2$-type $CeNi_2As_2$ is not strong, with a moderately enhanced Sommerfeld coefficient $\gamma_0 = 69$ mJ/mol K^2 and a relatively low Kondo scale $T_K \sim 4$ K. On the other hand, a huge frustration parameter $f = \theta_W/T_N$ is obtained, and a frustration-distortion picture was then proposed. The latter highlights the important role of Ce-$4f$ electrons in magnetic frustrations. Therefore, the $ThCr_2Si_2$-type $CeNi_2As_2$ provides a new candidate for the research of frustration-induced magnetic and structure transitions and calls for more investigations.

II. EXPERIMENT

High-purity single crystal of $ThCr_2Si_2$-type $CeNi_2As_2$ was grown by the NaAs flux method. CeAs, NiAs, and NaAs were presynthesized as mentioned elsewhere.[14,15] CeAs, NiAs, CeO_2,[16] and Ni were weighted in the ratio of 1:1:1:1, thoroughly ground in an argon-filled glove box. The mixture was then put into a Ta tube, together with 15 molar times of NaAs. After sealing the Ta tube by an arc melter, the tube was then sealed into a quartz tube filled with 0.2 bar argon gas. The quartz tube was heated up to 1493 K and kept at that temperature for 10 h, followed by slowly cooling down to 873 K in 10 days. The NaAs flux was dissolved by water in

 ©2012 American Physical Society

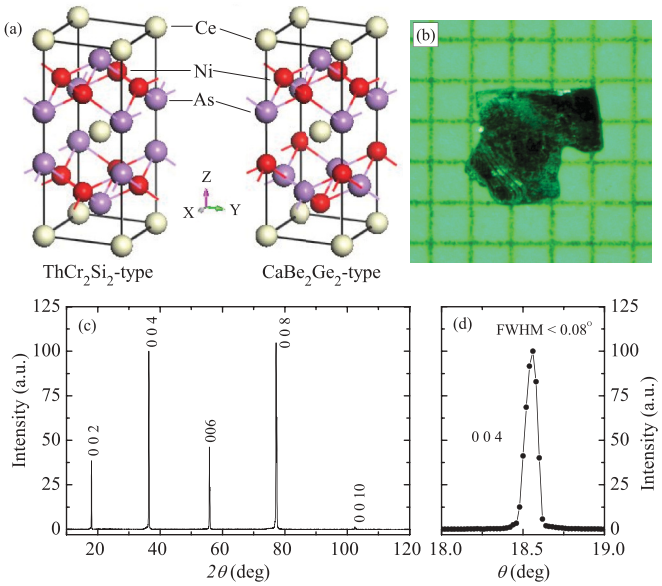

FIG. 1. (Color online) (a) Crystalline structure of $CeNi_2As_2$ of $ThCr_2Si_2$ type (left) and $CaBe_2Ge_2$ type (right). (b) A photo of a $CeNi_2As_2$ single crystal on millimeter grid paper. (c) XRD structure characterization of $CeNi_2As_2$ single crystal. Only (0 0 2l) peaks can be observed. (d) X-ray rocking curve through (0 0 4) reflection of $CeNi_2As_2$ single crystal.

a fume hood, and shining single crystals of $CeNi_2As_2$ with a typical size of $3 \times 3 \times 0.2$ mm^3 were picked out from the remaining dreg [see Fig. 1(b)].

The single-crystalline $CeNi_2As_2$ samples were checked by x-ray diffraction (XRD), performed on a PANalytical x-ray diffractometer (Empyrean Series 2) with Cu-$K_{\alpha 1}$ radiation at room temperature. Only (0 0 2l) peaks can be observed [Fig. 1(c)], confirming the $ThCr_2Si_2$-type crystalline structure. The full width at half maximum (FWHM) of the (0 0 4) peak in the rocking scan is less than 0.08°, demonstrating the goodness of sample quality [Fig. 1(d)]. We also performed Rietveld refinement[17] on the powder XRD data (not shown). The structural parameters are listed in Table I. The derived occupation of the Ni site is 0.856, close to the result of 0.86 obtained from energy-dispersive x-ray microanalysis (EDX) measurement. It is also comparable with previous literature.[13] The derived $a(b)$ and c are 4.0806(3) Å and 9.8843(7) Å, respectively. The small ratio $c/a = 2.43$, compared to 2.80 for $BaNi_2As_2$,[9] manifests a collapsed $ThCr_2Si_2$ structure.

Quantum Design (QD) magnetic property measurement system (MPMS-5) and physical property measurement system (PPMS-9) were used in the magnetization, transport, and specific-heat measurements. Ohmic contact was made with epoxy silver paste (Parts A + B), and annealed in Ar atmosphere at 573 K for 30 min. Resistivities of both in-plane (ρ_{ab}, $\mathbf{I} \parallel ab$) and out-of-plane (ρ_c, $\mathbf{I} \parallel c$) configurations were measured. Thermopower was measured by means of steady-state technique and a pair of differential type-E thermocouples was used to measure the temperature gradient. Specific heat was measured by heat pulse relaxation method in PPMS-9.

TABLE I. Lattice parameters of $CeNi_2As_2$ derived from Rietveld refinement based on space group $I4/mmm$. $a = b = 4.0806(3)$ Å, $c = 9.8843(7)$ Å, $\alpha = \beta = \gamma = 90°$.

Atom	Occupation	x	y	z
Ce	1.000	0	0	0
Ni	0.856	0	0.5	0.25
As	1.000	0	0	0.3654(3)

III. RESULTS AND DISCUSSION

The temperature-dependent magnetic susceptibility $\chi(T) = M/H$ and inverse magnetic susceptibility $1/\chi(T)$ along $\mathbf{B} \parallel \mathbf{c}$ and $\mathbf{B} \parallel \mathbf{ab}$ are displayed in Figs. 2(a) and 2(b), respectively. The magnitude of χ_c is almost the same as that of χ_{ab} at 400 K, but is 16 times larger at low temperature, indicative of increasing magnetic anisotropy. Both $\chi_c(T)$ and $\chi_{ab}(T)$ obey the Curie-Weiss law above 300 K. We fit the temperature-dependent susceptibility to the formula $\chi(T) = \frac{C}{T-\theta_W}$, with θ_W being the so-called Weiss temperature. The fit on the polycrystalline averaged susceptibility, defined as $\chi_{\rm avg} = (\chi_c + 2\chi_{ab})/3$, leads to the effective moment $\mu_{\rm eff} = 2.44\mu_B$. This value is close to but slightly less than $2.54\mu_B$, the effective moment of a free Ce^{3+}, manifesting the trivalent Ce ion and the nonmagnetic nature of the Ni sublattice. The high magnetic anisotropy is also reflected in the derived Weiss temperature $\theta_W^c = 32.2$ K and $\theta_W^{ab} = -165.9$ K. An AFM transition is signified by χ_c, which shows a sharp peak around 5 K and extrapolates to a very small magnitude in the zero-temperature limit. χ_{ab} also shows a peak at the same temperature, although the reduction of χ_{ab} after the formation of the AFM ordering is much weaker. The characteristic temperature of the AFM transition $T_N = 4.8$ K is then determined by the peak position in the $d\chi T/dT$ curves as shown in Fig. 2(c). We will find that this value is also consistent with the resistivity ($d\rho/dT$) and specific-heat (C) measurements. Figures 2(d) and 2(e) show the $\chi_c(T)$ and $\chi_{ab}(T)$ measured under various magnetic fields. It is interesting to notice that under increasing field, the AFM peak shifts to lower temperatures much faster for $\mathbf{B} \parallel \mathbf{c}$ than $\mathbf{B} \parallel \mathbf{ab}$. These observations suggest that the Ce^{3+} moments align along the c axis, while within the ab plane the correlation between the moments is much stronger. The deviation of $\chi(T)$ from Curie-Weiss law below 300 K is a sign of CEF effect and will be discussed later on.

Figure 3 shows isothermal magnetization $M(B)$ curves along $\mathbf{B} \parallel \mathbf{c}$ and $\mathbf{B} \parallel \mathbf{ab}$ directions. The most fascinating feature for $\mathbf{B} \parallel \mathbf{c}$ is that below T_N, $M(B)$ shows linear B dependence when $B < 2$ T, but undergoes a substantial increase at around 2.4 T before a saturation trend. $B_m = 2.36$ T is then defined at the magnetic field where the increasing rate of $M(B)$ reaches the maximum. A tiny hysteresis in $M(B)$ is observed near B_m, implying a weak first-order transition. Compared with $\mathbf{B} \parallel \mathbf{c}$, $M(B)$ for $\mathbf{B} \parallel \mathbf{ab}$ is linear and much smaller, which again provides evidence for the strong anisotropy in the magnetic correlation among Ce moments. This field-induced MMT may imply the competition between the in-plane correlation and Zeeman energy.

We now turn to the resistivity measurement. Both in-plane (ρ_{ab} with $\mathbf{I} \parallel \mathbf{ab}$) and out-of-plane ($\rho_c$ with $\mathbf{I} \parallel \mathbf{c}$) resistivities were measured, and the data are shown in Fig. 4(a).

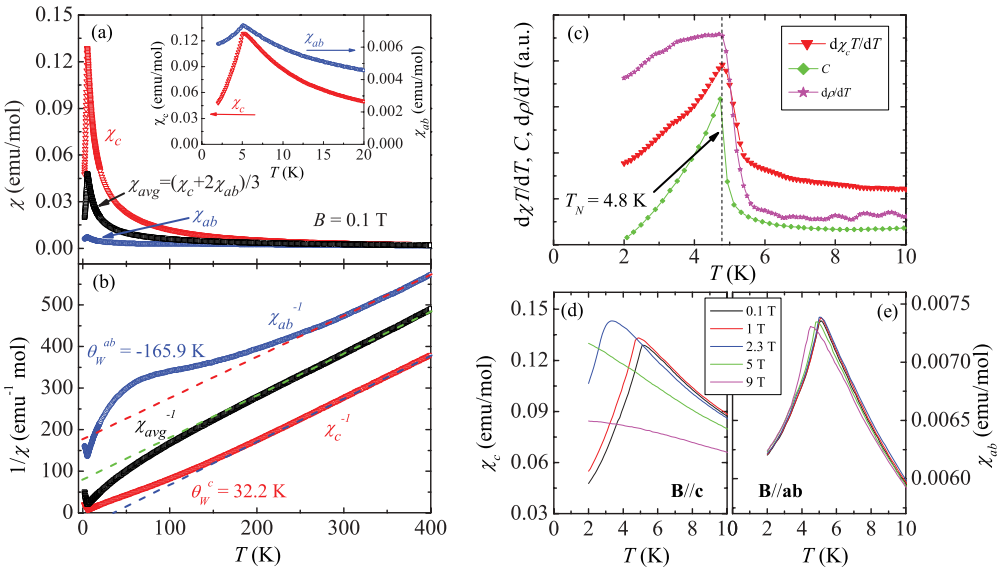

FIG. 2. (Color online) (a) Temperature-dependent magnetic susceptibility of $CeNi_2As_2$ measured at $B = 0.1$ T shown in **B** ∥ **c** (red) and **B** ∥ **ab** (blue) directions. Polycrystalline averaged susceptibility (black) was calculated by $\chi_{avg} = (\chi_c + 2\chi_{ab})/3$. (b) Shows inverse magnetic susceptibility. The dashed lines are guides to eyes of the Curie-Weiss fit. (c) Shows the definition of the AFM transition temperature T_N from $d\chi T/dT$, $C(T)$, and $d\rho/dT$. (d), (e) Exhibit the evolution of AFM peak in $\chi(T)$ under various magnetic fields for **B** ∥ **c** and **B** ∥ **ab**, respectively.

One should notice that the ratio ρ_c/ρ_{ab} at 400 K is 2.3, much smaller than that of the regular iron pnictide A-122 compounds[9,18–21] where the ratio is typically of the order of 10–100. It demonstrates more three-dimensional electronic property in $CeNi_2As_2$, and is consistent with the collapsed crystalline structure. For $T > 300$ K, ρ_{ab} shows weak metallic behavior, while in the $T < 300$ K region, ρ_{ab} increases with decreasing T, and a broad peak centered around 110 K is observed. Similar behavior is also observed in ρ_c whereas the broad peak position is relatively higher. The resistivity of its nonmagnetic reference $LaNi_2As_2$ was also measured (data not shown) on a polycrystalline sample, and no anomaly can be seen at this T region. Such broad peak in resistivity is then reminiscent of the CEF effect. Furthermore, a maximum in thermopower (see the inset of Fig. 4) observed around 155 K in $CeNi_2As_2$ allows us to get a rough estimate of the first excited Kramers doublet that is ∼310 K above the ground doublet. More detailed and accurate CEF analysis will be performed on the magnetic susceptibility fitting, seeing the context in the following. The anisotropic response to the CEF in resistivity [see also in Fig. 9(a)] may reflect the anisotropic hybridization strength of electron scattering to the CEF. Another prominent feature is observed below 50 K, where both ρ_{ab} and ρ_c increase rapidly, developing the sharp peaks near T_N. The $-\ln T$ behavior of low-temperature resistivity for $T_N < T < 50$ K is identified, revealing that $CeNi_2As_2$ belongs to a Kondo system with a weak Kondo scale $T_K \lesssim T_N$. Figures 4(b) and 4(c) show the isothermal in-plane resistivity ρ_{ab} versus the applied field perpendicular and parallel to the crystallography c axis, respectively. In the case of **B** ∥ **ab**, ρ_{ab} decreases slightly with B at $T = 10$ K $> T_N$. While at $T = 2$ K $< T_N$, a positive magnetoresistivity $\{MR$, defined as $MR = [\rho(B) - \rho(0)]/\rho(0)\}$ is clearly exhibited. This behavior is likely associated with the suppression of AFM ordering under the external field. The $\rho_{ab}(B)$ curves for **B** ∥ **c** are more intriguing: First, at T =10 K, ρ_{ab} decreases much faster for **B** ∥ **c** than that for **B** ∥ **ab**, providing further evidence that the magnetic easy axis to be the c axis. Second, at $T = 2$ K, $\rho_{ab}(B)$ substantially increases to a maximum near $B = 2.6$ T, and then decreases drastically. The turning point

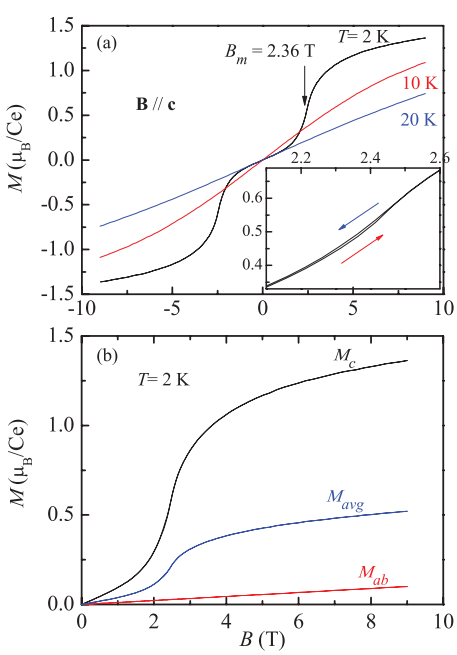

FIG. 3. (Color online) (a) Field dependence of isothermal magnetization of $CeNi_2As_2$ in **B** ∥ **c**, measured at 2, 10, and 20 K. Inset shows a tiny hysteresis near the MMT. (b) Shows $M(B)$ curves for both **B** ∥ **c** and **B** ∥ **ab** measured at 2 K. The polycrystalline averaged $M(B)$ is presented in (b).

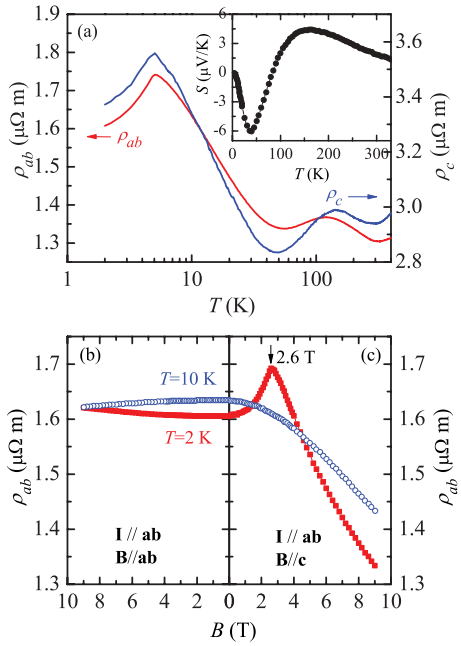

FIG. 4. (Color online) Transport properties of $CeNi_2As_2$. (a) Mainframe: temperature dependence of resistivity for both ρ_{ab} ($\mathbf{I} \parallel \mathbf{ab}$) and ρ_c ($\mathbf{I} \parallel \mathbf{c}$). Inset displays thermopower S as a function of T. (b), (c) ρ_{ab} as a function of magnetic field B for $\mathbf{B} \parallel \mathbf{ab}$ and $\mathbf{B} \parallel \mathbf{c}$, respectively.

of $\rho_{ab}(B)$ is apparently associated with the MMT observed in magnetization measurement discussed previously.

In Fig. 5, we present the specific heat divided by T as a function of temperature. A λ-shape peak is clearly seen at the transition temperature T_N, manifesting a second-order phase transition. Under the magnetic field, the specific-heat peak is suppressed to lower temperatures for $B < B_m$, indicating a fingerprint of the reduction of the AFM transition. When $B > B_m$, the sharp peak evolves with increasing magnetic field into a broad round peak moving to higher temperature. This Schottky-type peak in C/T under a field signifies a crossover from AFM ordering to paramagnetic state via Brillouin-type saturation, and is consistent with the magnetic properties

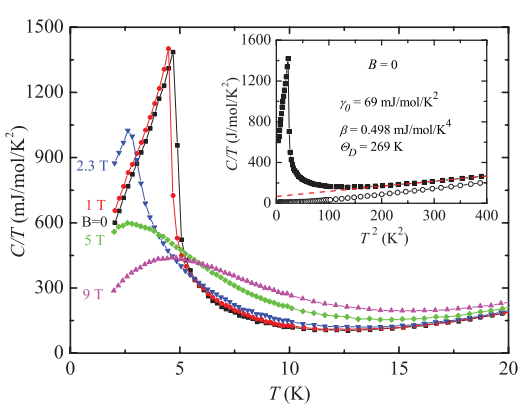

FIG. 5. (Color online) Specific heat of $CeNi_2As_2$ as a function of temperature, measured at various magnetic fields $\mathbf{B} \parallel \mathbf{c}$. Inset displays C/T versus T^2 to estimate the Sommerfeld coefficient γ_0. The solid symbols represent $CeNi_2As_2$, while open ones represent $LaNi_2As_2$.

measurement. We also plot the C/T versus T^2 in the inset of Fig. 5. The Sommerfeld coefficient $\gamma_0 \sim 69$ mJ/mol K^2 is then estimated by linearly extrapolating to the zero temperature. This moderately enhanced Sommerfeld coefficient manifests the correlation effect contributed from the Ce-4f electrons. The slope of the linear extrapolation is $\beta = 0.498$ mJ/mol K^4, and this leads to the Debye temperature $\Theta_D = 269$ K. Due to short-range order or CEF effects mentioned above, this estimate of Θ_D may have some uncertainty. A more reliable estimate of Θ_D may come from $LaNi_2As_2$ (polycrystal), where similar analysis leads to $\Theta_D = 256$ K.

In order to identify the Ce-4f-electron contribution to the specific heat, we consider the quantity $C_{\mathrm{mag}} = C_{\mathrm{Ce}}$-$C_{\mathrm{La}}$ as shown in Fig. 6(a), where C_{La} is the specific heat of $LaNi_2As_2$. It is expected that the difference C_{mag} is mainly due to the magnetic contribution because $LaNi_2As_2$ is nonmagnetic and isostructural to $CeNi_2As_2$. As expected, a sharp specific-heat jump for C_{mag} appears at T_N. The jump at T_N is $\Delta C_{\mathrm{mag}}\,|_{T=T_N} \sim$ 6 J/mol K. From this value, the Kondo scale could be roughly estimated as $T_K \sim 4$ K.[22] The magnetic entropy gain (S_m) was calculated by integrating C_{mag}/T over T. We found that S_m reaches 65% of $R \ln 2$ at T_N, and recovers this value at 19 K. This suggests that the observed anomaly in specific heat arises from the AFM ordering of Ce^{3+} moment in a two-degenerated ground state. Since T_K is low, the reduction of entropy gain at T_N should be mainly attributed to the short-range ordering or correlation of the Ce^{3+} moments above T_N, rather than the Kondo effect. The short-range ordering is also manifested by a noticeable broad tail in C_{mag} above T_N extending to about 20 K [see Fig. 6(a)]. A broad peak centered at around 160 K can also be observed on $C_{\mathrm{mag}}(T)$, which should be ascribed to the Schottky anomaly caused by the thermal population of CEF levels [see also in the inset of Fig. 6(a), where S_m substantially increases and reaches $R \ln 4$ near 150 K].

In Ce-contained compounds, the D_{4h} ($I4/mmm$) point symmetry requires a CEF Hamiltonian written as

$$\mathscr{H}_{\mathrm{CEF}} = B_2^0 O_2^0 + B_4^0 O_4^0 + B_4^4 O_4^4, \tag{1}$$

where B_l^m ($l = 2,\ 4,\ m = 0,\ 4$) are the CEF parameters, while O_l^m are Steven's operators.[23,24] In addition, the Zeeman interaction and exchange interaction should also be taken into account,

$$\mathscr{H}_{Zee} = -g\mu_B \mathbf{J} \cdot \mathbf{B}, \tag{2}$$

$$\mathscr{H}_{ex} = -\sum_{\langle i,j \rangle} J_{ex}^{\perp}\left(S_i^x S_j^x + S_i^y S_j^y\right) + J_{ex}^{\parallel} S_i^z S_j^z, \tag{3}$$

in which x, y, and z correspond to the crystallographic a, b, and c, where $g = \frac{6}{7}$ is the Landé factor of Ce^{3+} ions, $J_{ex}^{\perp}$ and $J_{ex}^{\parallel}$ are the components of the nearest-neighbor exchange interaction with Ce^{3+} moment perpendicular and parallel to the c axis, respectively. Combination of Eqs. (1), (2), and (3) allows us to get the expressions of inverse susceptibility,[25,26] i.e.,

$$\frac{1}{\chi_c} = \frac{1}{C}\left(T + \frac{j(j+1)}{3} J_{ex}^{\parallel} + \frac{(2j-1)(2j+3)}{5} B_2^0\right), \tag{4}$$

$$\frac{1}{\chi_{ab}} = \frac{1}{C}\left(T + \frac{j(j+1)}{3} J_{ex}^{\perp} - \frac{(2j-1)(2j+3)}{10} B_2^0\right) \tag{5}$$

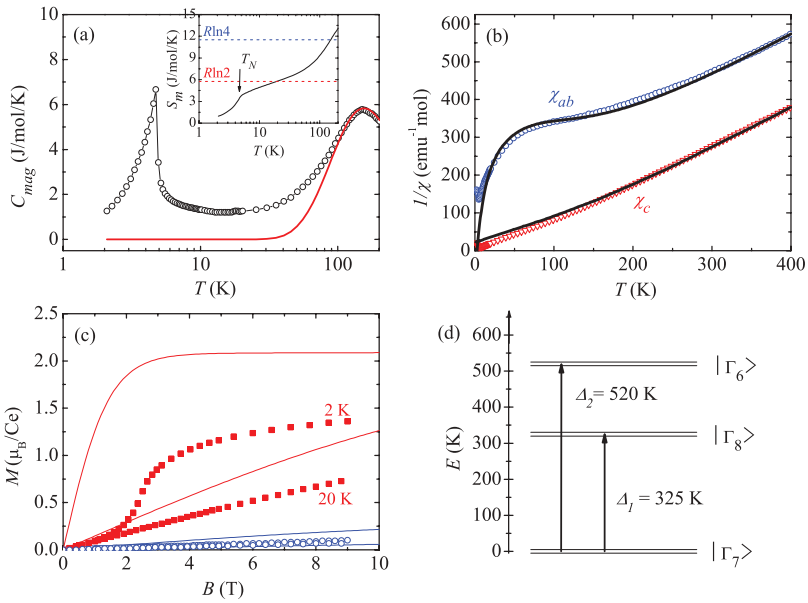

FIG. 6. (Color online) (a) Magnetic specific heat $C_{\rm mag}$, derived from $C_{\rm Ce}$-$C_{\rm La}$. Solid line represents the three-level Schottky anomaly fit based on the CEF model, where $\Delta_1 = 325$ K and $\Delta_2 = 520$ K. Inset of (a) shows the integrated entropy as a function of T, the two horizontal dashed lines stand for $R\ln 2$ and $R\ln 4$, respectively. (b) The inverse susceptibility (open symbols) and calculated curves (solid lines). (c) Experimental (symbols) and calculated (solid lines) isothermal magnetization at 2 and 20 K. Data for $\mathbf{B} \parallel \mathbf{c}$ are colored with red (solid squares), while $\mathbf{B} \parallel \mathbf{ab}$ are in blue (open circles). (d) Schematic sketch of CEF energy levels for Ce^{3+} ion in $CeNi_2As_2$.

with $j = \frac{5}{2}$ being the total angular momentum for Ce^{3+}. The experimental data of $1/\chi_c$ and $1/\chi_{ab}$ can be well reproduced by this model as shown in Fig. 6(b), with the best-fitted CEF parameters B_l^m as well as the CEF energy levels and eigenstates being listed in Table II. The ground state has a twofold degeneracy and takes the form $|\Gamma_7\rangle = \alpha_1 |\pm\frac{5}{2}\rangle + \alpha_2 |\mp\frac{3}{2}\rangle$ with $\alpha_1^2 + \alpha_2^2 = 1$. The calculated exchange interactions are $J_{ex}^{\parallel} = 9.18$ K and $J_{ex}^{\perp} = -23.1$ K, respectively, manifesting anisotropic magnetic couplings. The broad peak in $C_{\rm mag}(T)$ can also be well described by Schottky anomaly formula with energy excitations $\Delta_1 = 325$ K and $\Delta_2 = 520$ K, and the result is shown in Fig. 6(a). A schematic sketch of the CEF split is presented in Fig. 6(d). We should point out that a direct relation[27] of the paramagnetic Curie temperatures with the CEF parameter B_2^0, viz., $\theta_W^{ab} - \theta_W^c = \frac{3}{10} B_2^0 (2j-1)(2j+3)$, will lead to $B_2^0 = 20.6$ K that does not satisfy all the measured physical properties. We attributed this inconsistency to the neglect of the exchange interactions which play an important role in determining the ground state of this CEF splitting.[25]

Above, CEF analysis also allows calculating the spatial distribution of the $4f$-electron charge density[28] $\langle\Gamma_7|\,\rho_{4f}(\mathbf{r})\,|\Gamma_7\rangle$. In Fig. 7(a), we display the isosurface plot (namely, the electron cloud) of the $4f$ electron for a Ce^{3+} ion surrounded by the CEF in the $ThCr_2Si_2$-type $CeNi_2As_2$. The calculation was done at $T = 0.1$ K. It is evident that the electron cloud has deformed severely from the spherical shape, and is highly accumulated on the four corners which are along the Ce-As bonds, manifesting the hybridization between Ce-$4f$ and As-$4p$ orbitals. Another profound feature is that the Ce-$4f$ electron cloud is highly "squeezed" along the z axis (please note the dimensions of x, y, and z axes). It is well known that the topology of charge density is closely associated with the magnetic anisotropy. Due to the spin-orbit coupling, the orientation of the magnetic moment is coupled to the orientation of the $4f$ charge. In the CEF theory, this anisotropy is mainly governed by the Stevens factor α_j.[24,28] In the case of Ce^{3+} ions, the negative $\alpha_j = -5.7143 \times 10^{-2}$ favors the magnetic easy axis to be parallel along the "squeezed" direction. This result reinforces the previous statement that the Ce^{3+} moments are aligned along the c axis. Under a magnetic field $\mathbf{B} \parallel \mathbf{c}$, the electron cloud is further squeezed along the z axis [see Fig. 7(b)], and thus stabilizes the original magnetic easy axis. In contrast, an external field $\mathbf{B} \parallel \mathbf{ab}$ elongates the electron cloud along the z direction [see Fig. 7(c)], and consequently the magnetic moments will be rotated to the ab plane.

However, we notice that the CEF model does not perfectly reproduce the isothermal magnetization measured at low temperatures [see Fig. 6(c)]. For example, in the case of $\mathbf{B} \parallel \mathbf{c}$,

TABLE II. CEF parameters, energy levels, and wave functions in $CeNi_2As_2$ at zero magnetic field.

CEF parameters						
	$B_2^0 = -28.2$ K,	$B_4^0 = 0.106$ K,	$B_4^4 = 1.63$ K			
Energy levels and eigenstates						
E(K)	$\lvert\frac{5}{2},+\frac{5}{2}\rangle$	$\lvert\frac{5}{2},+\frac{3}{2}\rangle$	$\lvert\frac{5}{2},+\frac{1}{2}\rangle$	$\lvert\frac{5}{2},-\frac{1}{2}\rangle$	$\lvert\frac{5}{2},-\frac{3}{2}\rangle$	$\lvert\frac{5}{2},-\frac{5}{2}\rangle$
0	−0.9907	0	0	0	0.1362	0
0	0	−0.1362	0	0	0	0.9907
325	0.1362	0	0	0	0.9907	0
325	0	0.9907	0	0	0	0.1362
520	0	0	1	0	0	0
520	0	0	0	1	0	0

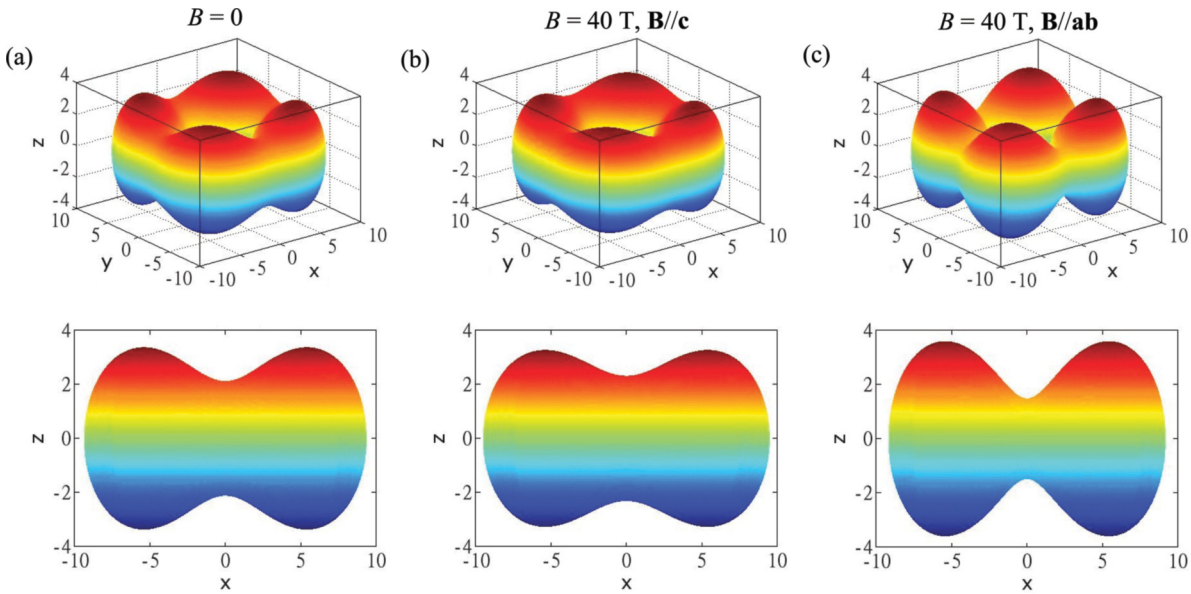

FIG. 7. (Color online) Isosurface plot of $4f$ charge density for a Ce^{3+} ion surrounded by CEF in $CeNi_2As_2$. Calculated at $T = 0.1$ K, (a) $B = 0$, (b) $B = 40$ T, $\mathbf{B} \parallel \mathbf{c}$, and (c) $B = 40$ T, $\mathbf{B} \parallel \mathbf{ab}$. The lower diagrams are the projections to the xz plane.

one expects a saturated magnetic moment $M_c = \frac{6}{7} \times \frac{5}{2} = 2.14\mu_B/\text{Ce}$, while the experimental value is about $1.36\mu_B/\text{Ce}$ for $T = 2$ K and $B = 9$ T. Meanwhile, we also notice that the amplitude of Weiss temperatures is much larger than the AFM transition temperature. Especially for the in-plane Weiss temperature θ_W^{ab}, we obtain a huge ratio $f_{ab} = \theta_W^{ab}/T_N = 34.6$. Such a large value of f_{ab} reminds us of the magnetic frustration neglected in the previous CEF analysis. A schematic diagram of this magnetic frustration is shown in Fig. 8. Taking into account only the nearest-neighbor exchange interactions for both intralayer and interlayer, the magnetic coupling between Ce^{3+} moments is denoted by J_1 and J_2, respectively. From the CEF calculation, we have a negative intralayer coupling which is dominating in magnitude. It means that the Ce^{3+} moments should be antiferromagnetically ordered within the ab plane, as shown in Fig. 8(a). In this situation, the magnetic frustration stems from the J_1-J_2 competition for the moments in the two adjacent layers as within the extended unit cell.[29] We propose that a structural distortion from the high-temperature tetragonal to low-temperature orthorhombic phases may possibly take place to release this magnetic frustration, as shown in Fig. 8(b). The unit cell is then doubled and the lattice constants a and b are no longer equivalent. This frustration-induced distortion scenario is reminiscent to a similar scenario in the iron pnictides, where the structural distortion is possibly due to the J_1-J_2 magnetic frustration caused by the $3d$-electron moments.[30–32] What we need to emphasize here is that the proposed frustration-induced distortion in the present case is caused by the Ce-$4f$ electrons. With this consideration, the CEF Hamiltonian in the low-temperature orthorhombic phase can be written as

$$\mathscr{H}_{\text{CEF}} = B_2^0 O_2^0 + B_2^2 O_2^2 + B_4^0 O_4^0 + B_4^2 O_4^2 + B_4^4 O_4^4. \quad (6)$$

Consequently, the ground state will change into a mixed state like $|\Gamma\rangle_0 = \alpha_1 |\pm\frac{5}{2}\rangle + \alpha_2 |\mp\frac{3}{2}\rangle + \alpha_3 |\pm\frac{1}{2}\rangle$ with $\alpha_1^2 + \alpha_2^2 + \alpha_3^2 = 1$, and therefore a saturated magnetic moment smaller than $2.14\mu_B/\text{Ce}$ will be expected under a moderate magnetic field. This situation is similar to the case in $CeNiGe_3$ reported by Mun *et al.*[33] However, it is hard to get the B_l^m's for this new phase since the information is very limited.

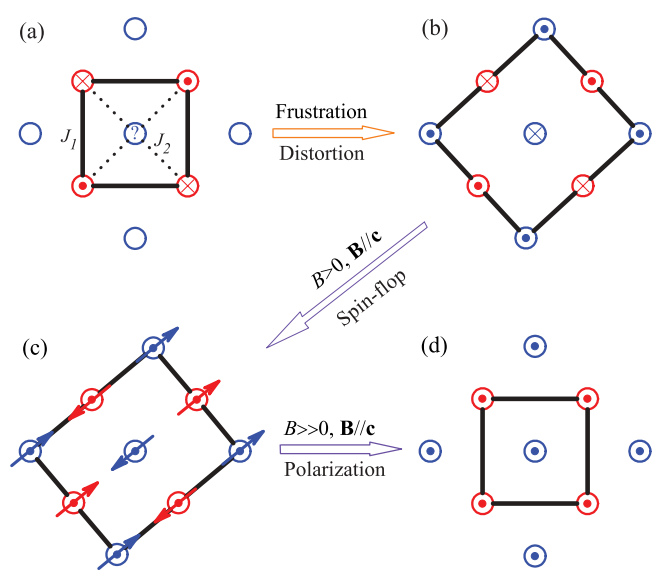

FIG. 8. (Color online) Schematic diagram of the magnetic structure of Ce^{3+} sublattice. The adjacent Ce^{3+} layers are denoted by colors, red and blue, while the orientations of a Ce^{3+} moment, up and down, are signified by "•" and "×." The thick lines characterize the unit cell. (a) Geometry frustration stems from the J_1-J_2 competition in the tetragonal phase, and tiny structure distortion may take place, which will lead to an orthorhombic phase as shown in (b). (c) Spin-flop transition happens when a field $\mathbf{B} \parallel \mathbf{c}$ is applied, which enhances the structure distortion. The arrows display the projection of the Ce^{3+} moment in the ab plane. (d) Geometry frustration reduces when Ce^{3+} moments are well polarized in the high-field limit.

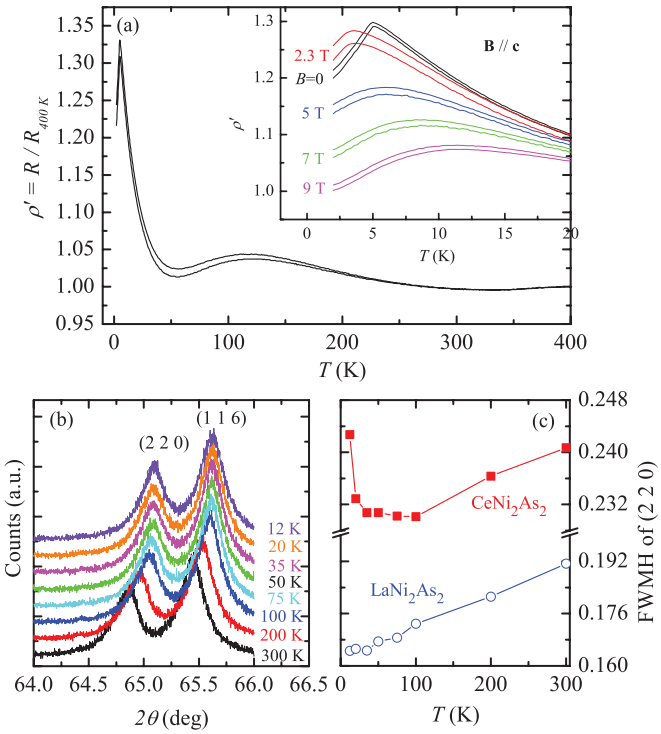

FIG. 9. (Color online) (a) Anisotropic in-plane resistivity of $CeNi_2As_2$, measured in van der Pauw's method. Inset displays this anisotropy under various field. (b) LTXRD patterns of $CeNi_2As_2$ powders. The two observed peaks are indexed as (2 2 0) and (1 1 6). (c) Temperature dependence of FWHM of (2 2 0) peak. For comparison, the result of $LaNi_2As_2$ is also shown.

To obtain more evidences for the structural distortion, we sought for the possible resistivity anisotropy in the ab plane by performing the $\rho_{a'}$-$\rho_{b'}$ measurement using the van der Pauw method[34] (please note that here $\mathbf{a}'$ and $\mathbf{b}'$ stand for two perpendicular directions in the ab plane, not necessarily the crystallographic $\mathbf{a}$ and $\mathbf{b}$). The measurement was carried out on a piece of square platelike single crystal, and $R_{a'}$ and $R_{b'}$ were measured via switching the direction of electrical current. To compare their temperature dependence, the normalized resistivity $\rho' = R/R_{400\,\mathrm{K}}$ is used, and the result is displayed in Fig. 9(a). Above 200 K, $\rho'_{a'}(T)$ and $\rho'_{b'}(T)$ overlap well, while below 200 K, a discrepancy between them is observed. It should be pointed out that this result was reproduced for many times on different batches of single crystals. The discrepancy becomes more evident with decreasing temperature, exhibiting the increasing anisotropy in the ab plane. It is worth emphasizing that this discrepancy between $\rho'_{a'}$ and $\rho'_{b'}$ can be enlarged under a moderate magnetic field $\mathbf{B} \parallel \mathbf{c}$ and reaches a maximum near B_m before it starts to decrease with further increased B [see the inset of Fig. 9(a)]. Combined with the MMT observed in isothermal magnetization displayed in Fig. 3, we argue that such field dependent $\rho'_{a'}$-$\rho'_{b'}$ may be related to the field-induced spin-flop transition. As is elucidated in Fig. 8(c), under a moderate magnetic field $\mathbf{B} \parallel \mathbf{c}$, the balance between the Zeeman energy and the AFM intralayer coupling requires that the Ce^{3+} magnetic moments gradually lie down to the ab plane. This will then further enhance the structural distortion as well as the resistivity anisotropy in the ab plane. When the external field is large enough, all the magnetic moments tend to be polarized, and thus the frustration decays with the increasing field.

The frustration-distortion scenario can be further tested by the low-temperature x-ray diffraction (LTXRD) experiment on the $CeNi_2As_2$ powder samples. We focused on the angular range $64^\circ \leqslant 2\theta \leqslant 66^\circ$, where only the (2 2 0) and (1 1 6) peaks can be observed. The data were collected at different temperatures down to 12 K, the lowest temperature of our equipment. All the collected LTXRD patterns are displayed in Fig. 9(b). We find that both (2 2 0) and (1 1 6) peaks shift to the right-hand side when cooling down, suggesting a shrinkage of the crystalline lattice, although for $T < 100$ K, this shrinkage becomes very weak. We fit all these LTXRD patterns to a combination of two Gaussian functions, through which the FWHM of (2 2 0) peak is derived as shown in Fig. 9(c). The initial reduction of the FWHM with decreasing temperature should be attributed to the slowing down of crystalline lattice oscillation. To our interest, an upturn of the FWHM is clearly seen when $T < 100$ K, and especially for $T < 20$ K, the FWHM increases rapidly with decreasing temperature, although we are not able to see the split of (2 2 0) peak directly. Such steep increase of the FWHM signals a tiny structural distortion or a precursor to that happened below T_N. In order to confirm the relevance of this behavior to the $4f$-electron magnetism, we also measured the FWHM of the $LaNi_2As_2$ compound [see Fig. 9(c)]. We find that the FWHM of $LaNi_2As_2$ drops monotonically with T down to the lowest temperature, in striking contrast to $CeNi_2As_2$. The significant distinction between the two cases again reinforces the frustration-distortion possibility driven by the $4f$ electrons.

We should remark that the structural distortion induced by the magnetic frustration of $4f$ electrons is in general small or even tiny. One reason is that the energy scale for magnetic couplings is smaller than that in the iron pnictides. Another reason is that the next-nearest-neighbor coupling J_3 between the Ce moments (within the same layer of the Ce sublattice as denoted in Ref. 29), which is neglected in the previous discussions, may also play some role. Although being small, J_3 usually competes with both J_1 and J_2 and may lead to incommensurate magnetic fluctuations.[29] Since a precise magnetic structure in $CeNi_2As_2$ is not easy to be determined by static magnetization and transport measurements, more investigations such as neutron scattering experiment are required to settle this issue.

Finally, we note that $CeNi_2P_2$, the counterpart compound to $CeNi_2As_2$, behaves as a typical Kondo lattice metal.[12] This fact demonstrates that the chemical "pressure," induced by replacing As with smaller isovalent P,[32,35] promisingly acts as an effective controlling parameter to tune the competition between the RKKY interaction and the Kondo coupling.[36] For the rare-earth iron pnictides, such competition is much involved and complicated, however, mainly due to the emergent magnetic order of the iron $3d$ electrons.[29] Owing to the absence of magnetism in the Ni sublattice, the Ce-Ni–based compounds have shown great advantage in studying the Ce-$4f$-electron correlation.[14,33,37,38] This also accounts to the fact that the $CaBe_2Ge_2$-type $CeNi_2As_2$ is a nonmagnetic Kondo lattice because the Kondo coupling is largely enhanced by one of the inverted NiAs layer. Compared with all these cases,

the $ThCr_2Si_2$-type $CeNi_2As_2$ has a relatively small Kondo coupling but a moderately strong magnetic frustration. The role played by strong magnetic frustration on the quantum phase transition, in the Kondo lattice in particular, remains an interesting issue.[39–41] Therefore, the $ThCr_2Si_2$-type $CeNi_2As_2$ may provide a new material for the research of quantum phase transitions mediated by the $4f$-electron magnetic frustration.

IV. CONCLUSION

To conclude, we performed a systematic investigation on the magnetic properties and the CEF effect in the $ThCr_2Si_2$-type $CeNi_2As_2$ single crystals. We find that this $CeNi_2As_2$ compound is a highly anisotropic uniaxial antiferromagnet with $T_N = 4.8$ K. The Kondo effect is estimated to be not strong in this system, while the magnetic frustration of the Ce-$4f$ moments plays an important role. Pronounced CEF effect is observed in magnetic, transport, and thermodynamic measurements. Detailed calculations based on the CEF theory allow capturing the electronic and magnetic properties of $CeNi_2As_2$. A possible frustration-induced structural distortion due to the Ce-$4f$ electrons is suggested, which is in agreement with the in-plane resistivity anisotropy and low-temperature XRD measurements. While this issue is reminiscent of the frustration-induced distortion emergent in the iron pnictide superconductors due to the d-electron correlation, the origin of the structural distortion and its relationship with the magnetic frustration in the $4f$-electron systems still need to be clarified in the future.

ACKNOWLEDGMENTS

Y. Luo would like to show gratitude to H. Xing and C. Cao for helpful discussions. This work was supported by the National Basic Research Program of China (Grants No. 2011CBA00103, No. 2012CB927404, and No. 2010CB923003), the National Science Foundation of China (Grants No. 11190023 and No. 11174247), and the Fundamental Research Funds for the Central Universities of China. J. Dai was also supported by the Natural Science Foundation of Zhejiang Province (Grant No. Z6110033).

*zhuan@zju.edu.cn

[1] M. Rotter, M. Tegel, and D. Johrendt, Phys. Rev. Lett. **101**, 107006 (2008).
[2] T. Park, E. Park, H. Lee, T. Klimczuk, E. D. Bauer, F. Ronning, and J. D. Thompson, J. Phys.: Condens. Matter **20**, 322204 (2008).
[3] P. L. Alireza, Y. T. Chris Ko, J. Gillett, C. M. Petrone, J. M. Cole, S. E. Sebastian, and G. G. Lonzarich, J. Phys.: Condens. Matter **21**, 012208 (2008)
[4] A. S. Sefat, R. Jin, M. A. McGuire, B. C. Sales, D. J. Singh, and D. Mandrus, Phys. Rev. Lett. **101**, 117004 (2008).
[5] L. J. Li, Y. K. Luo, Q. B. Wang, H. Chen, Z. Ren, Q. Tao, Y. K. Li, X. Lin, M. He, Z. W. Zhu, G. H. Cao, and Z. A. Xu, New. J. Phys. **11**, 025008 (2009).
[6] Z. Ren, Q. Tao, S. Jiang, C. Feng, C. Wang, J. Dai, G. Cao, and Z. Xu, Phys. Rev. Lett. **102**, 137002 (2009).
[7] J. J. Ying, T. Wu, Q. J. Zheng, Y. He, G. Wu, Q. J. Li, Y. J. Yan, Y. L. Xie, R. H. Liu, X. F. Wang, and X. H. Chen, Phys. Rev. B **81**, 052503 (2010).
[8] W. H. Jiao, Q. Tao, J. K. Bao, Y. L. Sun, C. M. Feng, Z. A. Xu, I. Nowik, I. Felner, and G. H. Cao, Europhys. Lett. **95**, 67007 (2011).
[9] A. S. Sefat, M. A. McGuire, R. Jin, B. C. Sales, D. Mandrus, F. Ronning, E. D. Bauer, and Y. Mozharivskyj, Phys. Rev. B **79**, 094508 (2009).
[10] F. Steglich, J. Aarts, C. D. Bredl, W. Lieke, D. Meschede, W. Franz, and H. Schafer, Phys. Rev. Lett. **43**, 1892 (1979).
[11] W. Jeitschko, W. K. Hofmannt, and L. J. Terbuchte, J. Less-Common Met. **137**, 133 (1988).
[12] H. Suzuki, H. Abe, H. Kitazawa, and D. Schmitt, J. Alloys Compd. **323–324**, 520 (2001).
[13] E. H. El Ghadraoui, J. Y. Pivan, R. Guérin, O. Pena, J. Padiou, and M. Sergent, Mater. Res. Bull. **23**, 1345 (1988).
[14] Y. Luo, H. Han, H. Tan, X. Lin, Y. Li, S. Jiang, C. Feng, J. Dai, G. Cao, Z. Xu, and S. Li, J. Phys.: Condens. Matter **23**, 175701 (2010).
[15] J.-Q. Yan, S. Nandi, J. L. Zarestky, W. Tian, A. Kreyssig, B. Jensen, A. Kracher, K. W. Dennis, R. J. McQueeney, A. I. Goldman, R. W. McCallum, and T. A. Lograsso, Appl. Phys. Lett. **95**, 222504 (2009).
[16] The actual role of CeO_2 here is still unknown. We have tried this synthesis without CeO_2, but the product turns out to be of $CaBe_2Ge_2$-type $CeNi_2As_2$. Besides, the same synthesis on $LaNi_2As_2$ single crystal also failed.
[17] F. Izumi and K. Momma, Solid State Phenom. **130**, 15 (2007).
[18] X. F. Wang, T. Wu, G. Wu, H. Chen, Y. L. Xie, J. J. Ying, Y. J. Yan, R. H. Liu, and X. H. Chen, Phys. Rev. Lett. **102**, 117005 (2009).
[19] D. Wu, N. Barišić, N. Drichko, S. Kaiser, A. Faridian, M. Dressel, S. Jiang, Z. Ren, L. J. Li, G. H. Cao, Z. A. Xu, H. S. Jeevan, and P. Gegenwart, Phys. Rev. B **79**, 155103 (2009).
[20] G. Wu, H. Chen, T. Wu, Y. L. Xie, Y. J. Yan, R. H. Liu, X. F. Wang, J. J. Ying, and X. H. Chen, J. Phys.: Condens. Matter **20**, 422201 (2008).
[21] Y. Tomioka, S. Ishida, M. Nakajima, T. Ito, H. Kito, A. Iyo, H. Eisaki, and S. Uchida, Phys. Rev. B **79**, 132506 (2009).
[22] M. J. Besnus, A. Braghta, N. Hamdaoui, and A. Meyer, J. Magn. Magn. Mater. **104–107**, 1385 (1992).
[23] K. W. H. Stevens, Proc. Phys. Soc., London, Sect. A **65**, 209 (1952).
[24] M. T. Hutchings, *Solid State Physics: Advances in Research and Applications*, edited by F. Seitz and D. Turnbull (Academic, New York, 1964), Vol. 16, p. 227.
[25] P. Boutron, Phys. Rev. B **7**, 3226 (1973).
[26] B. K. Cho, B. N. Harmon, D. C. Johnston, and P. C. Canfield, Phys. Rev. B **53**, 2217 (1996).
[27] Y. L. Wang, Phys. Lett. A **35**, 383 (1971).
[28] E. Bauer and M. Rotter, in *Properties and Applications of Complex Intermetallics*, Book series on Complex Metallic Alloys, edited by Ester Belin-Ferre (World Scientific Publishing, Singapore, 2010), Vol. 3, Chap. 5.

[29]J. Dai, J. X. Zhu, and Q. Si, Phys. Rev. B **80**, 020505(R) (2009).
[30]C. Fang, H. Yao, W.-F. Tsai, J. P. Hu, and S. A. Kivelson, Phys. Rev. B **77**, 224509 (2008).
[31]C. Xu, M. Muller, and S. Sachdev, Phys. Rev. B **78**, 020501(R) (2008).
[32]J. Dai, Q. Si, J. X. Zhu, and E. Abrahams, Proc. Natl. Acad. Sci. USA **106**, 4118 (2009).
[33]E. D. Mun, S. L. Bud'ko, A. Kreyssig, and P. C. Canfield, Phys. Rev. B **82**, 054424 (2010).
[34]L. J. van der Pauw, Philips Res. Repts. **13**, 1 (1958).
[35]Y. Luo, Y. Li, S. Jiang, J. Dai, G. Cao, and Z. A. Xu, Phys. Rev. B **81**, 134422 (2010).
[36]S. Doniatch, Phys. B (Amsterdam) **91**, 231 (1977).
[37]Y. Luo *et al.* (unpublished).
[38]A. P. Pikul, U. Stockert, A. Steppke, T. Cichorek, S. Hartmann, N. Caroca-Canales, N. Oeschler, M. Brando, C. Geibel, and F. Steglich, Phys. Rev. Lett. **108**, 066405 (2012).
[39]Q. Si, Phys. Status Solidi B **247**, 476 (2010).
[40]P. Coleman and A. H. Nevidomskyy, J. Low Temp. Phys. **161**, 182 (2010).
[41]S. J. Yamamoto and Q. Si, J. Low Temp. Phys. **161**, 233 (2010).